




RESEARCH ARTICLE | APRIL 16 2018

## Extreme magnetoresistance and SdH oscillation in compensated semimetals of NbSb<sub>2</sub> single crystals

Lei Guo; Yu-Kuai Liu; Guan-Yin Gao; Ye-Yu Huang; Heng Gao ; Lei Chen; Weiyao Zhao; Wei Ren; Shi-Yan Li; Xiao-Guang Li ; Shuai Dong ; Ren-Kui Zheng



*J. Appl. Phys.* 123, 155103 (2018)

<https://doi.org/10.1063/1.5021637>



View  
Online



Export  
Citation

### Articles You May Be Interested In

Giant semiclassical magnetoresistance in high mobility TaAs<sub>2</sub> semimetal

*Appl. Phys. Lett.* (January 2016)

Electronic structure and open-orbit Fermi surface topology in isostructural semimetals NbAs<sub>2</sub> and W<sub>2</sub>As<sub>3</sub> with extremely large magnetoresistance

*Appl. Phys. Lett.* (March 2022)

Magneto-transport properties of proposed triply degenerate topological semimetal Pd<sub>3</sub>Bi<sub>2</sub>S<sub>2</sub>

*Appl. Phys. Lett.* (April 2018)



Journal of Applied Physics

## Special Topics Open for Submissions

[Learn More](#)

# Extreme magnetoresistance and SdH oscillation in compensated semimetals of NbSb<sub>2</sub> single crystals

Lei Guo,<sup>1,2,a)</sup> Yu-Kuai Liu,<sup>3,a)</sup> Guan-Yin Gao,<sup>4,b)</sup> Ye-Yu Huang,<sup>5</sup> Heng Gao,<sup>6</sup> Lei Chen,<sup>1,7</sup> Weiyao Zhao,<sup>1,7,b)</sup> Wei Ren,<sup>6</sup> Shi-Yan Li,<sup>5</sup> Xiao-Guang Li,<sup>4</sup> Shuai Dong,<sup>2</sup> and Ren-Kui Zheng<sup>1,b)</sup>

<sup>1</sup>State Key Laboratory of High Performance Ceramics and Superfine Microstructure, Shanghai Institute of Ceramics, Chinese Academy of Sciences, Shanghai 200050, China

<sup>2</sup>School of Physics, Southeast University, Nanjing 211189, China

<sup>3</sup>Department of Applied Physics, The Hong Kong Polytechnic University, Hong Kong, China

<sup>4</sup>Hefei National Laboratory for Physical Sciences at the Microscale and Department of Physics, University of Science and Technology of China, Hefei 230026, China

<sup>5</sup>State Key Laboratory of Surface Physics, Department of Physics, and Laboratory of Advanced Materials, Fudan University, Shanghai 200433, China

<sup>6</sup>International Centre for Quantum and Molecular Structures, Physics Department, Shanghai University, Shanghai 200444, China

<sup>7</sup>ISEM, Innovation Campus, University of Wollongong, Wollongong, New South Wales 2500, Australia

(Received 6 January 2018; accepted 31 March 2018; published online 16 April 2018)

Topological semimetals represent one of the most interesting classes of materials that continue to attract worldwide interest. Here, we report magnetotransport properties of MPn<sub>2</sub>-type (M = Nb, Ta; Pn = P, As, Sb) NbSb<sub>2</sub> single-crystal semimetals with a centrosymmetric C12/m1 space group, paramagnetic ground state, and non-saturation parabolic-like magnetoresistance. The NbSb<sub>2</sub> crystals show metallic conductivity down to 2 K and undergo a metal-to-insulator-like transition under a magnetic field  $B$  ( $B \geq 4$  T) and exhibit a resistivity plateau in the low-temperature region ( $T \leq 10$  K), where the value of resistivity strongly depends on the magnitude and direction of the magnetic field. Upon sweeping the magnetic field from 0 to 14.5 T in the transverse configuration at  $T = 1.5$  K, the NbSb<sub>2</sub> crystal shows a large positive magnetoresistance ( $4.2 \times 10^3\%$  at  $B = 14.5$  T) with Shubnikov–de Haas (SdH) oscillation. Hall measurements reveal that both the carrier compensation between electrons and holes and the high mobility and large mean free path of carriers contribute to the large magnetoresistance. Fast Fourier transform analyses of angle-resolved SdH oscillation indicate that the Fermi surface of the NbSb<sub>2</sub> crystal is quasi-two-dimensional with three-dimensional components. These findings, together with the theoretically calculated electronic band structure obtained within the framework of density functional theory, suggest that NbSb<sub>2</sub> is a good candidate compensated semimetal for further theoretical and experimental investigation of this family of materials. *Published by AIP Publishing.*

<https://doi.org/10.1063/1.5021637>

## I. INTRODUCTION

Magnetoresistance (MR), which describes materials' resistance responses to external magnetic fields, is not only one of the most important topics in condensed matter physics but also vital to practical applications in the field of memories, sensors, and spintronic devices. Since the findings of giant magnetoresistance (GMR) in magnetic multilayers and colossal magnetoresistance (CMR) in perovskite manganites, considerable attention has been paid to the development of new materials with larger MR effects or novel mechanisms. Recently, extremely large magnetoresistance (XMR) in nonmagnetic semimetals, which differs significantly from the GMR and CMR, was discovered in WTe<sub>2</sub> single crystals<sup>1–4</sup> whose XMR values increase linearly with the square of magnetic field  $B$  (i.e.,  $\text{XMR} \propto B^2$ ) and exhibit no sign of saturation up to  $B = 60$  T. Such an

XMR phenomenon has very recently been found in several families of single-crystal semimetals, e.g., NbP,<sup>5</sup> TaP,<sup>6</sup> NbAs,<sup>7</sup> TaAs,<sup>8</sup> Cd<sub>3</sub>As<sub>2</sub>,<sup>9,10</sup> ZrTe<sub>5</sub>,<sup>11</sup> PtBi<sub>2</sub>,<sup>12</sup> and ZrSiS,<sup>13</sup> which show chiral anomalous magnetotransport properties and a nontrivial Berry phase. They are classified as topological semimetals (TSMs) and have drawn unparalleled attention very recently.<sup>13–15</sup>

Analogous to the topological semimetals, the XMR effect has also been observed in a LaSb compound with a rock salt crystal structure,<sup>16</sup> which, however, shows XMR only in the transverse measurement configuration [i.e., the direction of magnetic field perpendicular to the direction of electric current ( $B \perp I$ )] and no negative MR can be observed in the longitudinal measurement configuration ( $B \parallel I$ ). Namely, the LaSb compound is absent of the so-called chiral anomalies in magnetotransport behaviors. Combining quantum oscillation of magnetoresistance and angle-resolved photoemission spectroscopy, Zeng *et al.*<sup>17</sup> found a perfect compensation between the densities of electrons and holes at low temperatures for LaSb crystals, which reasonably

<sup>a)</sup>L. Guo and Y.-K. Liu contributed equally to this work.

<sup>b)</sup>Electronic addresses: ggy@ustc.edu.cn; wz929@uowmail.edu.au; and zrk@ustc.edu

accounts for the XMR effect in this system. Meanwhile, isostructural semimetals such as the antiferromagnetic NdSb,<sup>18,19</sup> PrSb,<sup>20</sup> TmSb,<sup>21</sup> and the nonmagnetic LaBi,<sup>22–24</sup> YSb,<sup>25–28</sup> and niobium and tantalum dipnictides  $\text{MPn}_2$  ( $\text{M} = \text{Nb, Ta, Pn} = \text{P, As, Sb}$ )<sup>14,29–34</sup> family were studied to reveal their electronic band structures and origin of the XMR effects in these material systems. As of now, several mechanisms such as the field-induced changes in the Fermi surface,<sup>35</sup> electron-hole compensation effect,<sup>17</sup> nontrivial band topology,<sup>23</sup> and strong spin-orbital coupling<sup>4</sup> have been proposed to explain the non-saturating and near-quadratic XMR characteristics. Despite all these different mechanisms, it is generally agreed that the XMR effect is closely related to their novel electronic band structures and the Fermi surface which however still need to be further explored.

In this article, we studied the electronic transport properties of high quality  $\text{MPn}_2$ -type  $\text{NbSb}_2$  single-crystal semimetals using multi-band Hall fitting, angle-resolved quantum oscillation, and magnetotransport measurements. The  $\text{NbSb}_2$  crystal undergoes a metal-to-insulator-like transition under a magnetic field and exhibits a resistivity plateau in the low-temperature region, where the resistivity strongly depends on the magnitude and direction of magnetic field. Upon sweeping the magnetic field from 0 to 14.5 T at 1.5 K, we observed a non-saturated XMR of  $4.2 \times 10^3\%$  at 14.5 T and a Shubnikov-de Haas (SdH) oscillation. Hall measurements demonstrate that XMR arises from the electron-hole compensation effect and the high mobility and large mean free path of carriers. Angle-resolved SdH oscillation combined with fast Fourier transform (FFT) analyses reveals that the  $\text{NbSb}_2$  crystal possesses a quasi-two-dimensional Fermi surface with three-dimensional components.

## II. EXPERIMENTAL METHODS

High-quality  $\text{NbSb}_2$  single crystals were grown by the chemical vapor transport using iodine ( $\text{I}_2$ ) as a transport agent. Briefly, high-purity stoichiometric amount ( $\sim 1.5$  g) of Nb and Sb powder (200 mesh), together with  $\sim 10$  mg/ml iodine, are sealed in a quartz tube as starting materials. The crystal growth was carried out in a two-zone furnace between  $1000^\circ\text{C}$  (source) and  $1100^\circ\text{C}$  (sink) for 2 weeks. The chemical reaction follows the formula  $\text{NbSb}_2(s) + 3\text{I}_2(g) \rightleftharpoons \text{NbI}_4(g) + 2\text{SbI}(g)$ . Note that the antimony triiodide is unstable at high temperatures, leading to antimony monoiodide as the main gas intermediate compound.<sup>44</sup> The  $\text{NbSb}_2$  single crystals grow preferentially along the [010] direction, resulting in rodlike crystals with a typical size of  $1 \times 2 \times 1 \text{ mm}^3$  and shiny surfaces, as shown in the inset of Fig. 1(b).

The crystal structure of the single crystals was characterized by a PANalytical X'pert x-ray diffractometer equipped with  $\text{Cu K}\alpha_1$  radiation. The strong  $(00l)$  ( $l = 1, 2, 3, 4, 5$ ) diffraction peaks [Fig. 1(b)], together with the sharp rocking curve with a full width at half maximum (FWHM) of  $0.03^\circ$  [Fig. 1(c)], which was taken on the (003) diffraction peak, indicates high quality of the  $\text{NbSb}_2$  single crystal. High-resolution transmission electron microscopy (HRTEM) was performed using a Tecnai G2F20 S-Twin transmission electron microscope. Note that the electron beam is incident along the [010] crystallographic direction. The representative high-magnification image with atomic resolution shown in Fig. 1(d) shows interplanar lattice spacings of 0.716 and 0.444 nm along the [001] and [200] crystallographic directions, respectively, and an angle of approximately  $120^\circ$  between the [001] and [200] directions. These structural

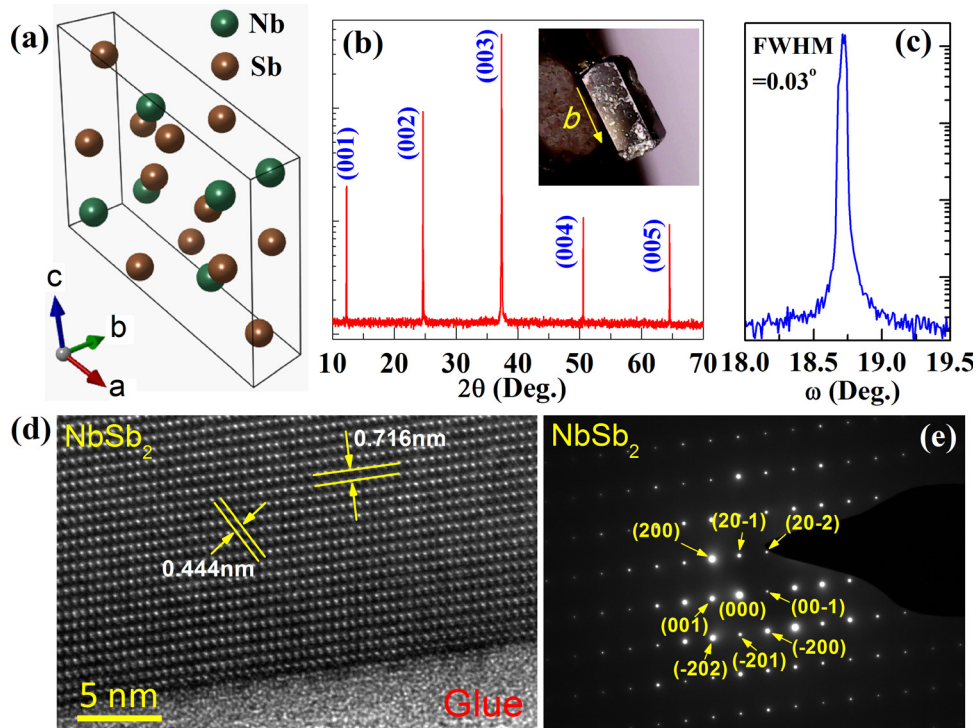


FIG. 1. (a) Crystal structure of  $\text{NbSb}_2$ . (b) XRD pattern of a  $\text{NbSb}_2$  crystal. Inset: a photograph of a  $\text{NbSb}_2$  crystal. (c) XRD rocking curve taken on the (003) diffraction peak. (d) HRTEM image with atomic resolution and (e) selected area electron diffraction pattern of a  $\text{NbSb}_2$  crystal.

characteristics agree well with the known crystal structure of NbSb<sub>2</sub><sup>36</sup> displayed in Fig. 1(a). The structural properties are further characterized by the selected area electron diffraction (SAED) pattern displayed in Fig. 1(e). The bright sharp spots can be well indexed according to the known crystal structure of NbSb<sub>2</sub>.<sup>36</sup> Energy dispersive X-ray spectroscopy (EDS) measurements using a Zeiss Supra 55 scanning electron microscope show that the Nb/Sb atomic ratio is 33.4/66.6, very close to that of stoichiometry NbSb<sub>2</sub>. These XRD, HRTEM, and EDS results demonstrate that the NbSb<sub>2</sub> single crystal is high quality, which provides good reliability for further investigations.

The electronic transport properties were measured by the standard four-probe method using a physical property measurement system (PPMS-9T, Quantum Design) and an Oxford <sup>4</sup>He cryostat with a 15 T magnet. Ohmic contacts were prepared on a fresh cleavage *ab* plane using room-temperature cured silver paste. The electric current is parallel to the *b* axis, while the direction of the magnetic field is parallel to the *c* axis of the crystal in the transverse magneto-transport measurements.

### III. RESULTS AND DISCUSSION

#### A. Temperature dependence of resistivity

As shown in Fig. 2(a), the resistivity ( $\rho$ ) under zero magnetic field ( $B = 0$  T) decreases monotonically with decreasing temperature down to 2 K, showing metallic behavior. The resistivity at 2 K becomes as low as approximately 10  $\mu\Omega$  cm, which is mainly due to the large mean free path of charge

carriers of the single crystal.<sup>13</sup> For  $T \leq 10$  K, the resistivity shows slight fluctuation, which is similar to that reported in the Cd<sub>3</sub>As<sub>2</sub><sup>9</sup> and ZrSiS<sup>13</sup> semimetals and might be explained in terms of the quantum ballistic transport. The residual resistivity ratio (RRR) is approximately 13.4 under zero magnetic field, suggesting good quality of the NbSb<sub>2</sub> crystal. Moreover, the resistivity in the temperature region from 10 to 50 K can be well fitted using the equation  $\rho(T) = \rho_0 + AT^n$  with  $n \sim 2.5$ . A similar phenomenon has been observed in compensated semimetals of LaSb<sup>16</sup> ( $n = 3$ ), LaBi<sup>35</sup> ( $n = 4$ ), and Dirac semimetals of ZrSiS<sup>13</sup> ( $n = 3$ ). This type of temperature dependence of resistivity, deviating from the pure electronic correlation-dominated scattering mechanism<sup>37</sup> ( $n = 2$ ), can be attributed to the interband electron-phonon scattering.<sup>13</sup>

Upon the application of magnetic fields, the resistivity in the low temperature region is significantly enhanced and retains metallicity for  $B \leq 3$  T [Fig. 2(b)]. However, for  $B \geq 4$  T, the resistivity shows a minimum at certain temperature ( $T_{\min}$ ) below which the resistivity increases with a further decrease in the temperature.  $T_{\min}$  increases monotonically with increasing magnetic fields [inset of Fig. 2(b)]. The relationship between  $T_{\min}$  and  $B$  can be described by the equation  $T_{\min} \sim (B - B_0)^{1/\nu}$ . The parameter  $\nu$  is  $\sim 2.3$ , which is close to that of compensated semimetals such as Bi ( $\nu = 2$ ),<sup>38</sup> WTe<sub>2</sub> ( $\nu = 2$ ),<sup>39</sup> and ZrSiS ( $\nu = 3$ ).<sup>13</sup> This type of magnetic-field-induced metal-to-insulator-like resistivity transition usually results from the gap opening at the band-touching points in semimetals.<sup>13,25</sup>

To confirm the gap opening effect associated with the temperature and magnetic field, we plot differential

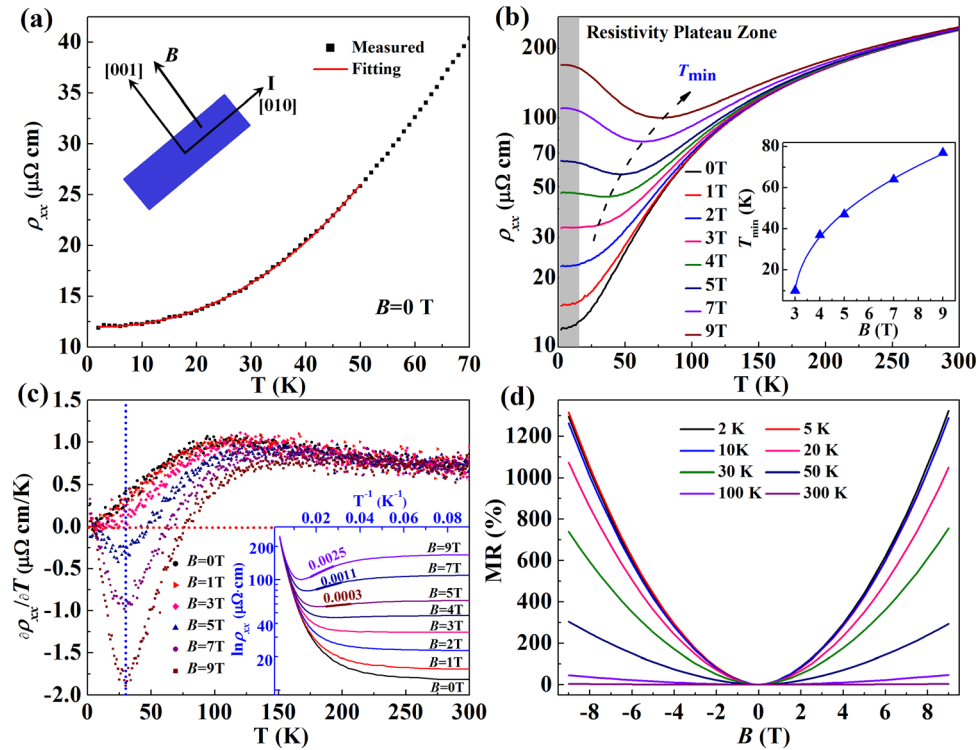


FIG. 2. (a) Zero-field resistivity (black point) and fitting results (red curve). Inset: schematic geometry of the directions of the magnetic field and the electric current. (b) Temperature dependence of resistivity under different magnetic fields, as measured using the schematic geometry shown in the inset of (a). The grey box shows the resistance plateau region. The black dashed arrow indicates the resistance minimum temperature ( $T_{\min}$ ). Inset:  $T_{\min}$  plotted as a function of magnetic field. (c)  $\partial\rho_{xx}/\partial T$  plotted as a function of temperature. Inset:  $\ln\rho$  plotted as a function of  $T^{-1}$ . (d) MR plotted as a function of magnetic field.



resistivity as a function of temperature ( $\partial\rho_{xx}/\partial T$ ) in Fig. 2(c). The metal-to-insulator transition temperature  $T_{\min}$ , corresponding to  $\partial\rho_{xx}/\partial T=0$  (see the red dashed guide line), can be readily obtained from Fig. 2(c), where one can find that  $T_{\min}$  increases with increasing magnetic field. In contrast, the onset temperature of the resistivity plateau ( $T_{\text{plateau}}$ ), where  $\partial\rho_{xx}/\partial T$  shows the minimum, remains unchanged with increasing magnetic fields. Furthermore, one may obtain the energy gap from the slopes of the logarithmic resistivity versus inverse temperature ( $\ln\rho_{xx} \sim 1/T$ ) curves within the linear regions,<sup>13,27</sup> as shown in the inset of Fig. 2(c). As the magnetic field increases from  $B=5$  to 7 and finally to 9 T, the gap increases from about 0.3 to 1.1 and finally to 2.5 meV. Obviously, the increase of the energy gap with increasing magnetic field is consistent with the variation of the metal-to-insulator transition temperature with the magnetic field.

### B. Extreme magnetoresistance and quantum oscillation

With the direction of the magnetic field perpendicular to the electric current direction and parallel to the  $c$  axis direction [see the inset of Fig. 2(a)], the metal-to-insulator transition becomes more and more pronounced, resulting in the XMR effect. Figure 2(d) shows the magnetic field dependence of XMR at different fixed temperatures from 2 to 300 K. With increasing magnetic field, XMR shows quasi-parabolic behaviors with no sign of saturation up to 9 T. For  $T=2$  K and  $B=9$  T, XMR is  $\sim 1300\%$ , which is comparable to the previously reported values of topological semimetals.<sup>5,13,35</sup> With increasing temperature, MR decreases to 3% at  $T=300$  K. For  $T>100$  K, the MR value seems quite similar to that of traditional metal materials. Interestingly, one could find a trace of resistivity oscillation in the low-temperature region, e.g.,  $T=2$  K. We employed an Oxford <sup>4</sup>He cryostat equipped with a 15 T magnet to further study the resistivity oscillation as a function of magnetic field up to 14.5 T at a constant temperature of 1.5, 2, 3, and 5 K, respectively [Fig. 3(a)]. Again, extremely large, non-saturating magnetoresistance (e.g.,  $4.2 \times 10^3\%$  at 1.5 K and

14.5 T) with Shubnikov-de Haas (SdH) oscillation appears when the magnetic field exceeds  $B=8.8$  T. The SdH oscillation amplitude  $[\Delta\rho = \rho - \langle\rho\rangle]$  is obtained by subtracting a smooth non-oscillatory background  $\langle\rho\rangle$  from the oscillating  $\rho$  and plotted against the inverse magnetic field in the inset of Fig. 3(a). The oscillation amplitude displays complex periodic behaviors and decreases with increasing temperature. Two frequencies of the SdH oscillation, i.e.,  $F_\alpha=65$  T and  $F_\beta=476$  T, are obtained by the fast Fourier transform (FFT) of  $\Delta\rho$  [Fig. 3(b)]. For SdH oscillation, the frequency  $F$  is proportional to the cross-section area of the Fermi surface ( $A_F$ ) that is normal to the magnetic field and can be described by the Onsager relationship,<sup>10</sup>  $F = (\phi_0/2\pi^2)A_F$ , where  $\phi_0$  is the magnetic flux quantum. The obtained cross sections are  $6.8 \times 10^{-3} \text{ \AA}^{-2}$  and  $4.99 \times 10^{-2} \text{ \AA}^{-2}$  for 65 and 476 T frequencies, respectively, indicating that these two Fermi pockets have different sizes, which is similar to the situation in the NbAs<sub>2</sub> single crystals.<sup>30</sup> Note that this small Fermi pocket for 65 T frequency obtained on this particular measurement configuration was yet not reported by the previously work.<sup>31</sup> Since the  $c$ -axis of our single crystal is exactly determined by x-ray diffraction, it is certain that the external magnetic field is along this direction. This small Fermi pocket perpendicular to the  $c$ -axis might show 2D behaviors, which is hard to detect from other crystallographic directions.

### C. Angular dependence of oscillation frequencies

To further understand the Fermi surface geometry, we performed angle-resolved SdH oscillation measurements. The MR curves and their FFT spectra for different directions of magnetic field are shown in Fig. 4(a). The lower inset of Fig. 4 shows the schematic geometry of the directions of the magnetic field with respect to that of the electric current. The parameter  $\theta$  is the angle between the  $c$  axis and the direction of the magnetic field. As the direction of the magnetic field rotates towards the electric current direction, MR decreases gradually; meanwhile, the frequency  $F_\alpha$  shifts to lower frequency and disappears at  $\theta = 30^\circ$ . The peak amplitude of  $F_\beta$  decreases until  $\theta = 30^\circ$  and vanishes for  $\theta > 30^\circ$ . It is worth

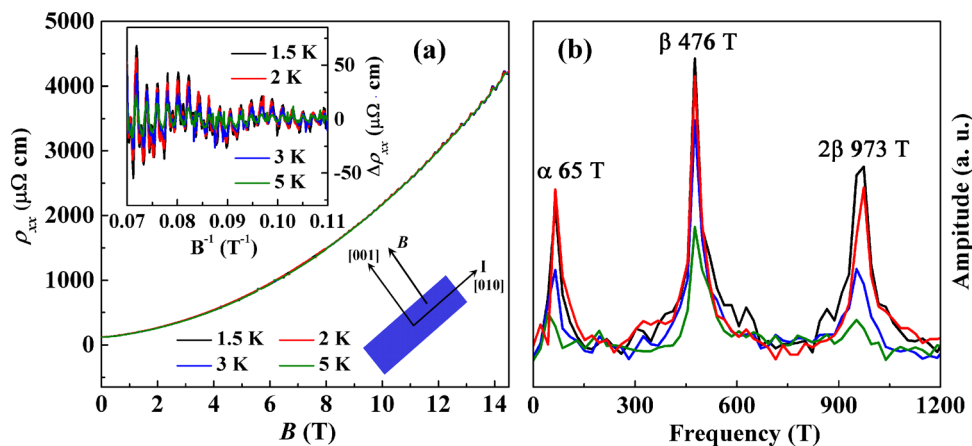


FIG. 3. (a) Resistivity plotted as a function of the magnetic field at different fixed temperatures for the NbSb<sub>2</sub> crystal. Insets: the oscillatory part of resistivity,  $\Delta\rho$ , at different fixed temperatures and the schematic geometry of the directions of the magnetic field and the electric current. (b) FFT spectra with two oscillation frequencies for the SdH oscillations.

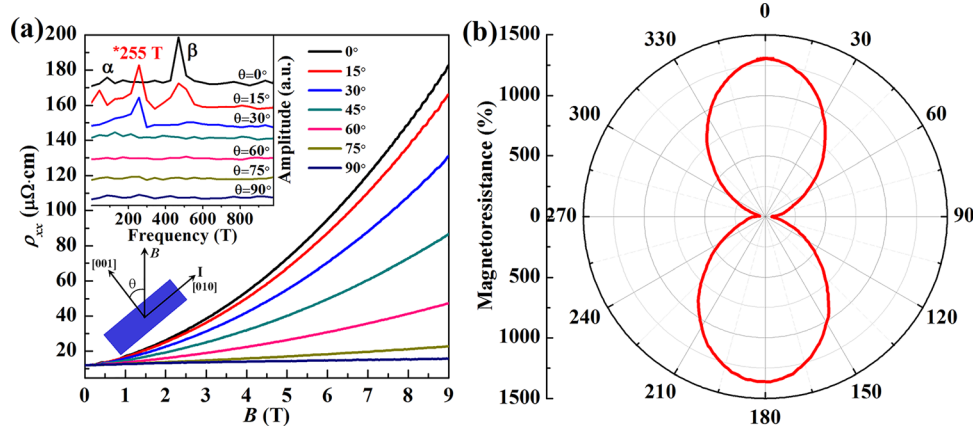


FIG. 4. (a) Resistivity plotted as a function of the magnetic field for seven angles with a gradient of  $15^\circ$ . The upper inset shows the FFT patterns of the oscillation parts extracted from the MR curves. The lower inset shows the schematic geometry of the directions of magnetic field with respect to that of the electric current. (b) Angular dependence of MR at  $T = 2$  K and  $B = 9$  T.

noting that with increasing  $\theta$  angle a new frequency at 250 T appears at  $15^\circ$ . This new frequency is the only oscillation frequency that is similar to that of  $\theta = 30^\circ$ . Once the angle  $\theta$  exceeds  $45^\circ$ , no clear oscillatory component can be detected in the measurements. Therefore, from the angular dependence of SdH oscillation one can find that there are three frequencies in the FFT spectra, indicating that the Fermi surface of the NbSb<sub>2</sub> crystal is quite complicate. Moreover, we measured angular dependence of the magnetoresistance and showed the results in Fig. 4(b). The dumbbell-shaped curve provides typical twofold anisotropy expected for a material with a quasi-two-dimensional electronic structure,<sup>40</sup> which further evidences the aforementioned quasi-two dimensional Fermi surface. The multi-frequency oscillation and their angle-dependent behaviors reveal the complicate morphology of the Fermi surface, which needs further measurements by angle-resolved photoemission spectroscopy.

#### D. Hall effect

To further understand the electronic transport behaviors of the NbSb<sub>2</sub> crystal in the XMR region, we performed Hall resistivity ( $\rho_{xy}$ ) measurements at  $T = 2, 25, 50$ , and  $75$  K [Fig. 5(a)]. It is evident that at those temperatures the slopes of  $\rho_{xy}$  versus  $B$  curves are negative, manifesting electron-dominant characteristics. The nonlinear tendency of the  $\rho_{xy}$

versus  $B$  curves suggests multi-band nature of the NbSb<sub>2</sub> crystal. It is known that for semimetals multi-conducting bands could contribute to the anomalous magnetotransport behaviors. We thus invoke the two-band model which consists of one electron- and one hole-band. The total conductivity tensor  $\sigma$  can be expressed in the complex representation<sup>1</sup>

$$\sigma = e \left[ \frac{n_e \mu_e}{(1 + i \mu_e B)} + \frac{n_h \mu_h}{(1 - i \mu_h B)} \right], \quad (1)$$

where  $n$  and  $\mu$  are the carrier density and carrier mobility, respectively. The subscripts  $e$  and  $h$  denote electrons and holes, respectively. Since  $\rho = \sigma^{-1}$ , the conductivity tensor  $\sigma$  in Eq. (1) can be transformed to resistivity tensor  $\rho$  whose real and imaginary parts  $\rho_{xx}$  and  $\rho_{xy}$ , respectively, can be written as

$$\rho_{xx}(B) = \text{Re}(\rho) = \frac{1}{e} \frac{(n_h \mu_h + n_e \mu_e) + (n_h \mu_e + n_e \mu_h) \mu_e \mu_h B^2}{(n_h \mu_h + n_e \mu_e)^2 + (n_h - n_e)^2 \mu_e^2 \mu_h^2 B^2}, \quad (2)$$

$$\rho_{xy}(B) = \text{Im}(\rho) = \frac{B}{e} \frac{(n_h \mu_h^2 - n_e \mu_e^2) + (n_h - n_e) \mu_e^2 \mu_h^2 B^2}{(n_h \mu_h + n_e \mu_e)^2 + (n_h - n_e)^2 \mu_e^2 \mu_h^2 B^2}. \quad (3)$$

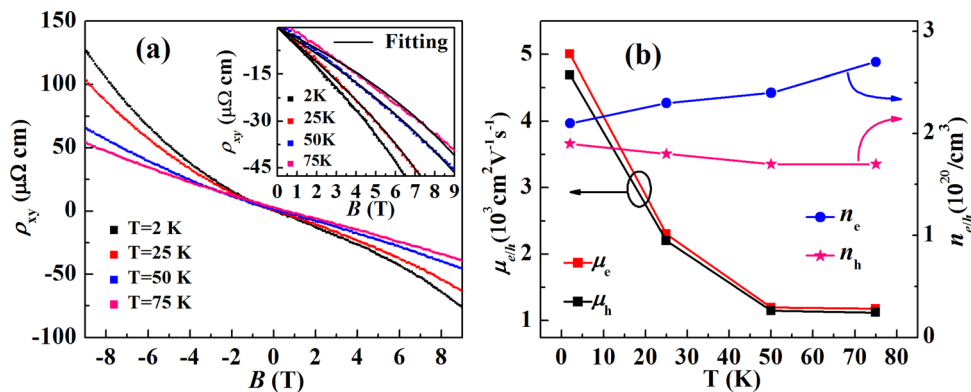


FIG. 5. (a) Hall resistivity plotted as a function of the magnetic field at different fixed temperatures. Inset: Fitting of Hall resistivity data at different temperatures. (b) Volume carrier density and mobility of electron- and hole-carriers as a function of temperature.

We fitted the  $\rho_{xy}$  data using Eq. (3) [inset of Fig. 5(a)] and obtained the fitting parameters  $n_e$ ,  $n_h$ ,  $\mu_e$ , and  $\mu_h$ , which are the carrier density and mobility of electrons and holes, respectively. The fitting parameters are displayed in Fig. 5(b). The electron and hole mobility  $\mu_e$  and  $\mu_h$  decrease with increasing temperature from 2 to 75 K, while the electron and hole carrier densities show a different variation trend with increasing temperature. Namely,  $n_e$  increases monotonically, while  $n_h$  decreases slightly with increasing temperature. Two important features could be found for the carrier density and mobility. (1) the carrier densities of electrons and holes are almost compensated at 2 K; (2) up to 75 K, the carrier mobility still retain a relatively high value of  $\sim 1.1 \times 10^3 \text{ cm}^2 \text{ V}^{-1} \text{ S}^{-1}$ , which is consistent with the non-saturated XMR feature of the NbSb<sub>2</sub> crystal.

#### IV. DISCUSSION

Previously, several mechanisms have been proposed to explain the extremely large and non-saturated MR in non-magnetic semimetals. One of the mechanisms is related to the massless Dirac fermions with a linear dispersion band structure.<sup>41,42</sup> However, this effect results in linear variation of XMR with the magnetic field,<sup>42</sup> which is apparently different from the parabolic like XMR behaviors in the NbSb<sub>2</sub> crystal. Thus, the band topology should not be the main mechanism that is responsible for the XMR of the NbSb<sub>2</sub> crystal. Another mechanism is involved with the carrier compensation effect which would result in the variation of MR with magnetic field in the form of the  $\text{MR} \sim B^2$  relationship. According to Eq. (2),  $\rho_{xx}(B)$  would be linearly proportional to  $B^2$  when  $(n_e - n_h)$  approaches zero. Using Hall measurements, we found that the carrier densities of electrons and holes almost compensate each other in the low-temperature region, supporting the carrier compensation effect as the underlying mechanism for the XMR. Moreover, within the framework of density functional theory our theoretically calculated relativistic electronic band structure and Fermi surface [Figs. S1(a) and S1(b), [supplementary material](#)] show that the NbSb<sub>2</sub> is a semimetal with electron and hole pockets around the L and F<sub>1</sub> points in the Brillouin Zone and there is a small gap with 9 meV along I-L due to the spin-orbital coupling effect. In addition, the high carrier mobility and the large mean free path of charge carriers would also contribute to the XMR.<sup>43</sup>

On the other hand, angle-resolved SdH oscillations suggest a complicate Fermi surface of the NbSb<sub>2</sub> crystal in which three Fermi pockets could be deduced. (1) The 65 T Fermi pocket is two-dimensional, whose oscillation frequency shifts with the rotation of the direction of magnetic field; (2) the 476 T Fermi pocket remains more-or-less constant upon the rotation of the direction of the magnetic field, which implies a three-dimensional character; (3) at  $\theta = 15$  and  $30^\circ$ , a new Fermi pocket with 255 T frequency occurs, which also shows a three-dimensional character. It is thus concluded that the Fermi surface of the NbSb<sub>2</sub> crystal shows a quasi-two-dimensional character with three-dimensional contribution. More theoretical and experimental efforts are needed to further probe into the quantum transport properties

of NbSb<sub>2</sub> crystals to reveal their topological properties, electronic structure, and Fermi surface.

#### V. CONCLUSIONS

To summarize, we have grown high-quality NbSb<sub>2</sub> single crystals which crystallize in the monoclinic structure with a C12/m1 space group. Electronic transport measurements show that the NbSb<sub>2</sub> crystal exhibits metallic conductivity down to 2 K and a resistivity plateau below  $T = 10$  K, whose magnitude is strongly enhanced by a magnetic field with its direction perpendicular to the electric current direction. Upon sweeping the magnetic field at  $T = 1.5$  K, the NbSb<sub>2</sub> crystal shows large positive magnetoresistance ( $4.2 \times 10^3\%$ ) with quantum oscillation in the high-field region. Hall measurements demonstrate that the densities of electron and hole almost compensate each other at  $T = 2$  K. This feature, together with the high mobility and large mean free path of the carriers, can reasonably explain the large magnetoresistance of the NbSb<sub>2</sub> crystal. Multi-frequency and angle-resolved SdH oscillation combined with fast Fourier transform analyses reveals a quasi-two-dimensional Fermi surface with three-dimensional components of the NbSb<sub>2</sub> crystals. All these findings, together with the theoretically calculated electronic band structure and Fermi surface, demonstrate that NbSb<sub>2</sub> is one of the good candidates for further theoretical and experimental investigation of this family of semimetals.

#### SUPPLEMENTARY MATERIAL

See the [supplementary material](#) for theoretical calculation of the relativistic electronic band structure and Fermi surface of the NbSb<sub>2</sub> single crystal.

#### ACKNOWLEDGMENTS

This work was supported by the National Natural Science Foundation of China (Grant Nos. 51572278, 51502129, 51332007, and 51672171) and the National Basic Research Program of China (Grant Nos. 2016YFA0300103, 2015CB921201, and 2015CB921600). The Eastern Scholar Program from the Shanghai Municipal Education Commission, the Fok Ying Tung Education Foundation, the Special Program for Applied Research on Super Computation of the NSFC-Guangdong Joint Fund (the second phase), and the China Scholarship Council are also acknowledged.

<sup>1</sup>M. N. Ali, J. Xiong, S. Flynn, J. Tao, Q. D. Gibson, L. M. Schoop, T. Liang, N. Haldolaarachchige, M. Hirschberger, N. P. Ong, and R. J. Cava, *Nature* **514**, 205–208 (2014).

<sup>2</sup>Y. K. Luo, H. Li, Y. M. Dai, H. Miao, Y. G. Shi, H. Ding, A. J. Taylor, D. A. Yarotski, R. P. Prasankumar, and J. D. Thompson, *Appl. Phys. Lett.* **107**, 182411 (2015).

<sup>3</sup>P. L. Cai, J. Hu, L. P. He, J. Pan, X. C. Hong, Z. Zhang, J. Zhang, J. Wei, Z. Q. Mao, and S. Y. Li, *Phys. Rev. Lett.* **115**, 057202 (2015).

<sup>4</sup>J. Jiang, F. Tang, X. C. Pan, H. M. Liu, X. H. Niu, Y. X. Wang, D. F. Xu, H. F. Yang, B. P. Xie, F. Q. Song, P. Dudin, T. K. Kim, M. Hoesch, P. K. Das, I. Vobornik, X. G. Wan, and D. L. Feng, *Phys. Rev. Lett.* **115**, 166601 (2015).

<sup>5</sup>C. Shekhar, A. K. Nayak, Y. Sun, M. Schmidt, M. Nicklas, I. Leermakers, U. Zeitler, Y. Skourski, J. Wosnitza, Z. K. Liu, Y. L. Chen, W. Schnelle,

- H. Borrmann, Y. Grin, C. Felser, and B. H. Yan, *Nat. Phys.* **11**, 645–649 (2015).
- <sup>6</sup>F. Arnold, C. Shekhar, S. C. Wu, Y. Sun, R. D. Dos Reis, N. Kumar, M. Naumann, M. O. Ajeesh, M. Schmidt, A. G. Grushin, J. H. Bardarson, M. Baenitz, D. Sokolov, H. Borrmann, M. Nicklas, C. Felser, E. Hassinger, and B. H. Yan, *Nat. Commun.* **7**, 11615 (2016).
- <sup>7</sup>N. J. Ghimire, Y. K. Luo, M. Neupane, D. J. Williams, E. D. Bauer, and F. Ronning, *J. Phys.: Condens. Matter* **27**, 152201 (2015).
- <sup>8</sup>B. Q. Lv, H. M. Weng, B. B. Fu, X. P. Wang, H. Miao, J. Ma, P. Richard, X. C. Huang, L. X. Zhao, G. F. Chen, Z. Fang, X. Dai, T. Qian, and H. Ding, *Phys. Rev. X* **5**, 031013 (2015).
- <sup>9</sup>T. Liang, Q. Gibson, M. N. Ali, M. H. Liu, R. J. Cava, and N. P. Ong, *Nat. Mater.* **14**, 280–284 (2015).
- <sup>10</sup>L. P. He, X. C. Hong, J. K. Dong, J. Pan, Z. Zhang, J. Zhang, and S. Y. Li, *Phys. Rev. Lett.* **113**, 246402 (2014).
- <sup>11</sup>R. Y. Chen, Z. G. Chen, X. Y. Song, J. A. Schneeloch, G. D. Gu, F. Wang, and N. L. Wang, *Phys. Rev. Lett.* **115**, 176404 (2015).
- <sup>12</sup>W. S. Gao, N. N. Hao, F. W. Zheng, W. Ning, M. Wu, X. D. Zhu, G. L. Zheng, J. L. Zhang, J. W. Lu, H. W. Zhang, C. Y. Xi, J. Y. Yang, H. F. Du, P. Zhang, Y. H. Zhang, and M. L. Tian, *Phys. Rev. Lett.* **118**, 256601 (2017).
- <sup>13</sup>R. Singha, A. K. Pariari, B. Satpati, and P. Mandal, *Proc. Natl. Acad. Sci. U.S.A.* **114**, 2468–2473 (2017).
- <sup>14</sup>R. Lou, Y. F. Xu, L. X. Zhao, Z. Q. Han, P. J. Guo, M. Li, J. C. Wang, B. B. Fu, Z. H. Liu, Y. B. Huang, P. Richard, T. Qian, K. Liu, G. F. Chen, H. M. Weng, H. Ding, and S. C. Wang, *Phys. Rev. B* **96**, 241106 (2017).
- <sup>15</sup>B. Q. Lv, Z. L. Feng, Q. N. Xu, X. Gao, J. Z. Ma, L. Y. Kong, P. Richard, Y. B. Huang, V. N. Strocov, C. Fang, H. M. Weng, Y. G. Shi, T. Qian, and H. Ding, *Nature* **546**, 627–631 (2017).
- <sup>16</sup>F. F. Tafti, Q. D. Gibson, S. K. Kushwaha, N. Haldolaarachchige, and R. J. Cava, *Nat. Phys.* **12**, 272–277 (2016).
- <sup>17</sup>L. K. Zeng, R. Lou, D. S. Wu, Q. N. Xu, P. J. Guo, L. Y. Kong, Y. G. Zhong, J. Z. Ma, B. B. Fu, P. Richard, P. Wang, G. T. Liu, L. Lu, Y. B. Huang, C. Fang, S. S. Sun, Q. Wang, Y. G. Shi, H. M. Weng, H. C. Lei, K. Liu, S. C. Wang, T. Qian, J. L. Luo, and H. Ding, *Phys. Rev. Lett.* **117**, 127204 (2016).
- <sup>18</sup>M. Neupane, M. M. Hosen, I. Belopolski, N. Wakeham, K. Dimitri, N. Dhakal, J. X. Zhu, M. Z. Hasan, E. D. Bauer, and F. Ronning, *J. Phys.: Condens. Matter* **28**, 23LT02 (2016).
- <sup>19</sup>N. Wakeham, E. D. Bauer, M. Neupane, and F. Ronning, *Phys. Rev. B* **93**, 205152 (2016).
- <sup>20</sup>F. Wu, C. Y. Guo, M. Smidman, J. L. Zhang, and H. Q. Yuan, *Phys. Rev. B* **96**, 125122 (2017).
- <sup>21</sup>Y. Y. Wang, H. Zhang, X. Q. Lu, L. L. Sun, S. Xu, Z. Y. Lu, K. Liu, S. Zhou, and T. L. Xia, *Phys. Rev. B* **97**, 085137 (2018).
- <sup>22</sup>X. H. Niu, D. F. Xu, Y. H. Bai, Q. Song, X. P. Shen, B. P. Xie, Z. Sun, Y. B. Huang, D. C. Peets, and D. L. Feng, *Phys. Rev. B* **94**, 165163 (2016).
- <sup>23</sup>J. Nayak, S. C. Wu, N. Kumar, C. Shekhar, S. Singh, J. Fink, E. D. Rienks, G. H. Fecher, S. P. Parkin, B. H. Yan, and C. Felser, *Nat. Commun.* **8**, 13942 (2017).
- <sup>24</sup>R. Lou, B. B. Fu, Q. N. Xu, P. J. Guo, L. Y. Kong, L. K. Zeng, J. Z. Ma, P. Richard, C. Fang, Y. B. Huang, S. S. Sun, Q. Wang, L. Wang, Y. G. Shi, H. C. Lei, K. Liu, H. M. Weng, T. Qian, H. Ding, and S. C. Wang, *Phys. Rev. B* **95**, 115140 (2017).
- <sup>25</sup>O. Pavlosiuk, P. Swatek, and P. Wiśniewski, *Sci. Rep.* **6**, 38691 (2016).
- <sup>26</sup>J. F. He, C. F. Zhang, N. J. Ghimire, T. Liang, C. J. Jia, J. Jiang, S. J. Tang, S. D. Chen, Y. He, S. K. Mo, C. C. Hwang, M. Hashimoto, D. H. Lu, B. Moritz, T. P. Devereaux, Y. L. Chen, J. F. Mitchell, and Z. X. Shen, *Phys. Rev. Lett.* **117**, 267201 (2016).
- <sup>27</sup>N. J. Ghimire, A. S. Botana, D. Phelan, H. Zheng, and J. F. Mitchell, *J. Phys.: Condens. Matter* **28**, 235601 (2016).
- <sup>28</sup>Q. H. Yu, Y. Y. Wang, R. Lou, P. J. Guo, S. Xu, K. Liu, S. Wang, and T. L. Xia, *Europhys. Lett.* **119**, 17002 (2017).
- <sup>29</sup>Z. J. Yuan, H. Lu, Y. J. Liu, J. F. Wang, and S. Jia, *Phys. Rev. B* **93**, 184405 (2016).
- <sup>30</sup>Y. Y. Wang, Q. H. Yu, P. J. Guo, K. Liu, and T. L. Xia, *Phys. Rev. B* **94**, 041103 (2016).
- <sup>31</sup>K. F. Wang, D. Graf, L. J. Li, L. M. Wang, and C. Petrovic, *Sci. Rep.* **4**, 7328 (2014).
- <sup>32</sup>B. Shen, X. Y. Deng, G. Kotliar, and N. Ni, *Phys. Rev. B* **93**, 195119 (2016).
- <sup>33</sup>C. C. Xu, J. Chen, G. X. Zhi, Y. K. Li, J. H. Dai, and C. Cao, *Phys. Rev. B* **93**, 195106 (2016).
- <sup>34</sup>Y. K. Li, L. Li, J. L. Wang, T. T. Wang, X. F. Xu, C. Y. Xi, C. Cao, and J. H. Dai, *Phys. Rev. B* **94**, 121115 (2016).
- <sup>35</sup>S. S. Sun, Q. Wang, P. J. Guo, K. Liu, and H. C. Lei, *New J. Phys.* **18**, 082002 (2016).
- <sup>36</sup>A. Rehr and S. M. Kauzlarich, *Acta Crystallogr., Sect. C: Cryst. Struct. Commun.* **50**, 1177–1178 (1994).
- <sup>37</sup>J. M. Ziman, *Electrons and Phonons: The Theory of Transport Phenomena in Solids* (Oxford University Press, 1960).
- <sup>38</sup>Y. Kopelevich, J. C. M. Pantoja, R. R. da Silva, and S. Moehlecke, *Phys. Rev. B* **73**, 165128 (2006).
- <sup>39</sup>Y. L. Wang, L. R. Thoutam, Z. L. Xiao, J. Hu, S. Das, Z. Q. Mao, J. Wei, R. Divan, A. Luican-Mayer, and G. W. Crabtree, *Phys. Rev. B* **92**, 180402 (2015).
- <sup>40</sup>J. Hu, Z. J. Tang, J. Y. Liu, X. Liu, Y. L. Zhu, D. Graf, K. Myhro, S. Tran, C. N. Lau, J. Wei, and Z. Q. Mao, *Phys. Rev. Lett.* **117**, 016602 (2016).
- <sup>41</sup>J. G. Analytis, R. D. McDonald, S. C. Riggs, J. H. Chu, G. S. Boebinger, and I. R. Fisher, *Nat. Phys.* **6**, 960–964 (2010).
- <sup>42</sup>A. A. Abrikosov, *Phys. Rev. B* **58**, 2788 (1998).
- <sup>43</sup>F. Han, J. Xu, A. S. Botana, Z. L. Xiao, Y. L. Wang, W. G. Yang, D. Y. Chung, M. G. Kanatzidis, M. R. Norman, G. W. Crabtree, and W. K. Kwok, *Phys. Rev. B* **96**, 125112 (2017).
- <sup>44</sup>One of the main factors to grow high quality single crystal is the transport agent. The saturation pressure of antimony is quite low, e.g.,  $2.7 \times 10^{-3}$  Pa at 1100 K, which means that good transport agent is highly desired. In the single crystal growth process of transition metal antimonides, chlorine, and iodine, as well as antimony ( $\text{Sb}^{5+}$ )-chloride, are usually used as transport agents. Among them, iodine is the most popular one for its solid phase at room temperature and easy to remove from the mixture. In the high temperature region,  $\text{SbI}_3$  would increasingly decompose to  $\text{SbI}$ , resulting in  $\text{SbI}$  as the main intermediate compound. Here, we use the equivalent formula to simply represent the series chemical reactions in the sealed quartz tube.